Fine Chemical Engineering
https://ojs.wiserpub.com/index.php/FCE/

Research Article

Hydrogenation-Driven Phase and Morphology Changes in Ru-Doped TiO_2 Nanotubes

Elham Khorashadizade*, **Fatemeh Nasiri**

Pasargad Institute for Advanced Innovative Solutions (PIAIS), Tehran, Iran
E-mail: elham.khorashadizade@piais.ir

Received: 10 February 2025; **Revised:** 3 April 2025; **Accepted:** 15 April 2025

Graphical Abstract:

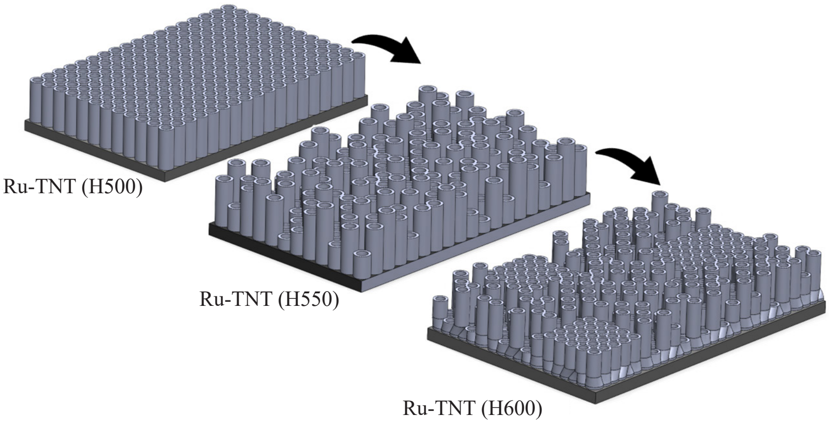

Abstract: A comprehensive understanding of the interplay between doping, thermal treatment, and structural evolution in titanium dioxide (TiO_2) is critical for optimizing its performance in photocatalysis and energy applications. While doping and hydrogenation have been extensively studied as independent processes, their combined effects on the structural and morphological evolution of TiO_2 nanotubes remain insufficiently explored. This study investigates the influence of hydrogenation temperature on ruthenium-doped TiO_2 nanotubes (Ru-TNTs) subjected to heat treatment at 500 °C, 550 °C, and 600 °C under an Ar/H_2 (90/10) atmosphere. Structural analysis reveals that increasing the hydrogenation temperature accelerates the anatase-to-rutile phase transition, induces lattice distortions, and promotes crystal growth, resulting in a reduction of the anatase phase fraction from 89.18% to 39.38%. High-resolution transmission electron microscopy (HRTEM) confirms these structural modifications, showing a transition from a well-defined crystalline lattice in Ru-TNTs hydrogenated at 500 °C to the formation of a disordered outer layer at 600 °C, consistent with X-ray diffraction (XRD) and field-emission scanning electron microscopy (FE-SEM) observations. Furthermore, microscopic analysis indicates significant morphological deformation with increasing temperature. These findings underscore the critical role of controlled hydrogenation in tailoring the structural and morphological properties

---

DOI: https://doi.org/10.37256/fce.6220256538

of Ru-TNTs, providing valuable insights for the development of advanced materials with enhanced photocatalytic and energy conversion efficiencies.

***Keywords*:** thermal hydrogenation, Ru-doped TiO_2 nanotubes, phase transformation, morphological alterations, reduction post-treatment

1. Introduction

Titanium dioxide (TiO_2) nanotubes have been the subject of extensive investigation due to their remarkable structural, optical, and photocatalytic properties, which make them ideal for applications such as water splitting, solar energy harvesting, and pollutant degradation.[1-4] Enhancing the performance of TiO_2 often involves doping with foreign elements and applying post-synthesis treatments.[5-7] Among these, ruthenium (Ru) doping combined with thermal hydrogenation has emerged as an effective method to modify the structural and electronic properties of TiO_2 nanotubes, thereby improving their stability and functionality under various operational conditions.[8,9]

Ru has been chosen as a dopant due to its ability to enhance electronic conductivity, stabilize the TiO_2 lattice, and facilitate controlled phase transitions.[10] Compared to other transition metals, Ru exhibits superior catalytic activity, electrical conductivity, and thermal stability, making it highly suitable for applications requiring long-term performance and high efficiency.[11]

Some studies have suggested that thermal hydrogenation does not induce significant changes in the XRD patterns of either doped or undoped TiO_2 nanotubes[12,13] with the anatase phase remaining stable at temperatures up to 800 °C in vacuum.[14] For instance, Schmuki's team indicated that the thermal hydrogenation process does not significantly affect the primary crystalline structure of TiO_2 nanotubes without doping.[13] The XRD analysis after post-treatment in an Ar/H_2 atmosphere confirmed the retention of well-crystallized anatase. Conversely, other studies have reported a shift toward higher 2θ values in doped samples, a trend that is consistent with our earlier observations.[8,15,16] Despite extensive research on defective TiO_{2-x} nanostructures, a critical knowledge gap remains regarding the combined influence of thermal hydrogenation and elemental doping on the anatase-to-rutile phase transition and morphological alteration.

This study systematically examines the impact of ruthenium (Ru) doping on the structural and thermal stability of TiO_2 nanotubes when subjected to hydrogenation at different temperatures (500 °C, 550 °C, and 600 °C) in a reductive Ar/H_2 atmosphere. Hydrogenation above 600 °C leads to electrode fragility and cracking in Ru-doped TiO_2 nanotubes. Under these conditions, phase transitions and lattice distortions may occur, potentially facilitating the formation of new crystal structures. Morphological changes induced by hydrogenation are analyzed using field emission scanning electron microscopy (FE-SEM) and high-resolution transmission electron microscopy (HRTEM). The findings provide deeper insights into the interplay between Ru doping, thermal hydrogenation, and TiO_2 phase stability, offering valuable guidance for optimizing these materials for photocatalysis and other energy applications.

2. Materials and methods

2.1 *Fabrication of Ru-doped TiO_2 nanotubes*

Intrinsically Ru-doped TiO_2 nanotube thin films were fabricated via the electrochemical anodization of a Ti-Ru alloy containing 0.2 atomic % Ru. Prior to the anodization process, the substrates underwent a thorough cleaning procedure that involved sequential ultrasonic treatment in acetone, ethanol, and deionized water, each for 15 minutes. This was followed by drying with nitrogen gas. Anodization was performed at 120 V using a high-voltage power supply in a two-electrode configuration for 2 hours. A platinum mesh served as the counter electrode, while the Ti-Ru alloy acted as the working electrode. The electrolyte used consisted of 0.2 M HF dissolved in 99 vol.% ethylene glycol. After anodization, the samples were rinsed with ethanol and dried with a nitrogen stream. To crystallize the as-formed Ru-doped TiO_2 nanotubes, the samples underwent annealing in air at a temperature of 450 °C for 1 hour (hereafter referred to as Ru-TNT).

2.2 *Thermal hydrogenation treatment*

The hydrogenated Ru-TNT samples were synthesized in a tube furnace under an Ar/H_2 atmosphere with a composition of 90/10 vol %. A schematic of the thermal hydrogenation process is shown in Figure 1. Initially, the furnace was purged with argon gas for 30 minutes at a flow rate of 14 mL min^{-1} to ensure an oxygen-free environment. The argon gas supply was then shut off, and the furnace was filled with the Ar/H_2 mixture for 10 minutes, maintaining the same flow rate of 14 mL min^{-1}. Subsequently, the fabricated nanostructures were annealed at predetermined temperatures (500, 550, and 600 °C) under the Ar/H_2 gas flow at a rate of 2.5 mL min^{-1} for one hour, yielding samples designated as Ru-TNT (H500), Ru-TNT (H550), and Ru-TNT (H600), respectively. Upon completing the reduction process and before opening the furnace, argon gas was reintroduced to prevent exposure of the reducing gas to ambient air, ensuring safety.

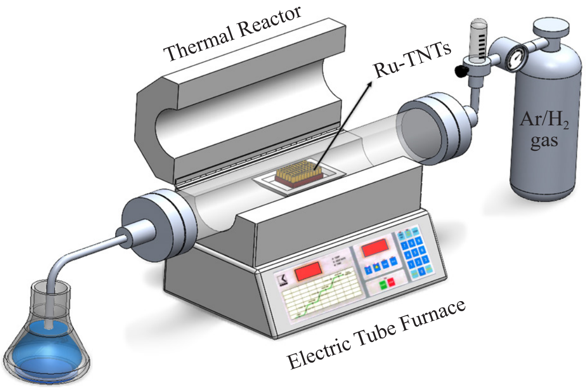

Figure 1. A schematic of thermal hydrogenation treatment of Ru-TNTs

2.3 *Characterizations: morphology and crystal structure*

Field-emission scanning electron microscopy (FE-SEM) was employed to analyze the surface morphology of the fabricated thin films. The crystal structure of the nanotube thin films was characterized using grazing incidence X-ray diffraction (GIXRD) with Cu K_α radiation (λ = 1.5406 Å). XRD scans were conducted over a 2θ range of 20-80° with a scanning rate of 0.05° per second. The crystallite size was estimated from the peak broadening of the XRD reflections, using the Scherrer formula as given by the following equation:[17]

$$D = \frac{K\lambda}{\beta \cos\theta} \tag{1}$$

where D represents the crystallite size, k is the dimensionless shape factor (set to 0.94 in this study),[18,19] λ is the wavelength of the X-ray radiation used, θ is the diffraction half angle, and β is the full width at half-maximum (FWHM) in radians, obtained from the XRD patterns of the anatase (101) and rutile (110) peaks.

The interplanar d-spacing, a fundamental property of crystalline materials, is determined using Bragg's law, given by the following equation:[20]

$$d = \frac{n\lambda}{2\sin\theta} \tag{2}$$

where n is order of diffraction (typically n = 1 for first-order diffraction), λ is the wavelength of the X-ray beam (in Å), and θ is the Bragg angle.

3. Results and discussions

3.1 *Crystalline phase transformation*

Figure 2a presents the grazing incidence X-ray diffraction (GIXRD) patterns of Ru-TNT samples hydrogenated at temperatures of 500, 550, and 600 °C, designated as Ru-TNT (H500), Ru-TNT (H550), and Ru-TNT (H600), respectively. The tetragonal anatase phase (space group I41/amd, JCPDS No. 21-1272)[21] is identified by sharp, characteristic peaks marked by black triangles (▼) in the GIXRD spectra. This phase is dominant in the sample hydrogenated at 500 °C (dark yellow line), where the intensity of the anatase peaks is higher, suggesting that at hydrogenation temperatures 50 °C above the annealing temperature, the TiO_2 nanotubes primarily maintain the anatase structure.

As the hydrogenation temperature increased, the intensity of the anatase peaks gradually decreased, particularly in the samples treated at 550 °C (red line) and 600 °C (blue line), indicating a transition from the anatase to the rutile phase.[22] The rutile phase is indicated by hollow triangles (▽) in the XRD spectra. In the XRD spectrum of Ru-TNT (H500), the (110) peak corresponding to the rutile TiO_2 phase at $2\theta = 27.47°$ appeared relatively weak, indicating that the rutile phase is present in only small amounts.

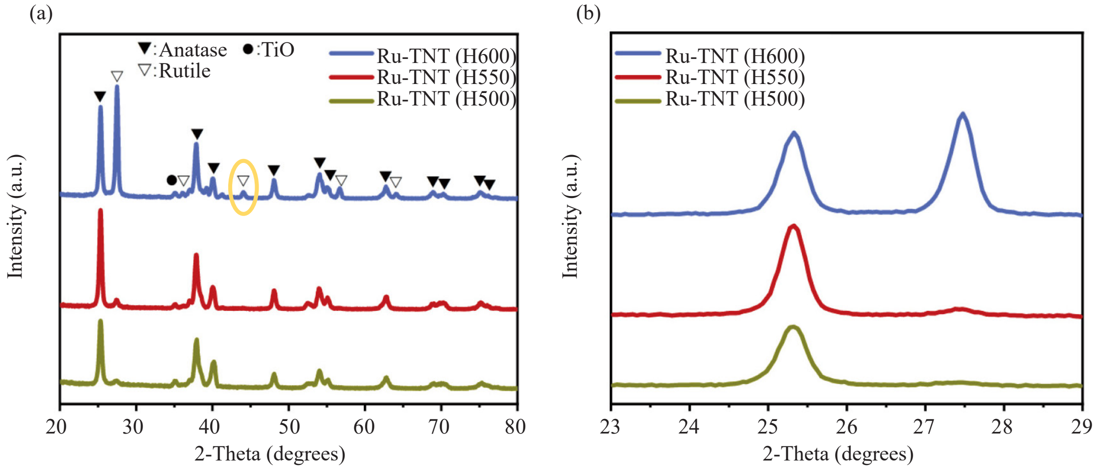

Figure 2. XRD patterns of Ru-doped TNTs subjected to thermal hydrogenation treatments at temperatures of 500, 550, and 600 °C are designated as Ru-TNT (H500), Ru-TNT (H550), and Ru-TNT (H600), respectively (a) $2\theta = 20\text{-}80°$ and (b) $2\theta = 23\text{-}29°$

However, as the hydrogenation temperature increased to 550 °C and 600 °C, the intensity of the (110) peak increased significantly. Figure 2b illustrates the 2θ angles in the range of 23° to 29°, using a higher magnification to clearly highlight the variations. The data in Figure 2a and b indicate that the (110) diffraction peak in the Ru-TNT (H600) sample is the most pronounced, suggesting that crystal growth predominantly occurs along this specific plane of rutile TiO_2.[23] These changes are attributed to the formation of a compact crystal lattice, which results from the removal of oxygen from the TiO_2 lattice in the Ar/H_2 medium, causing lattice deformation in the doped nanostructures.[8,24] Moreover, another diffraction peak corresponding to the (210) plane of rutile phase appeared at $2\theta = 43.98°$ in the XRD pattern of Ru-TNT (H600) sample. This peak is highlighted in yellow in Figure 2a. Additionally, the 3D waterfall plots of the samples in Figure 3 clearly show this peak in the XRD pattern of Ru-TNT (H600) at higher magnification.

When comparing our results to those of previous studies,[25-27] it is important to note that the synergistic effect of doping and thermal hydrogenation not only accelerates the anatase-to-rutile phase transformation but also induces distortion in the crystal lattice. This is particularly significant when examining the impact of thermal hydrogenation temperatures in an Ar/H_2 reductive atmosphere on the crystallite size of Ru-doped TiO_2 nanotubes based on X-ray diffraction data.

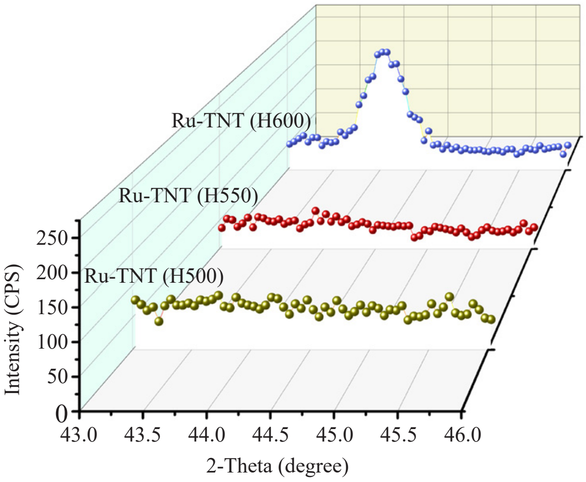

Figure 3. A 3D waterfall plot of XRD patterns for the Ru-TNT (H500), Ru-TNT (H550), and Ru-TNT (H600) samples within the 2θ range of 43° to 46° is provided to offer a more comprehensive perspective on this particular range

Table 1 presents a comparison of crystallite sizes (D) determined using the Scherrer equation (Equation (1)) and d-spacing (Equation (2)) for various hydrogenated samples. Furthermore, the positions of the (101) peaks related to the anatase phase, along with their FWHM values, have been analyzed and compared. For the Ru-TNT (H600) sample, data for both the (101) and the (110) diffraction peaks, corresponding to the anatase and rutile TiO_2 phases, respectively, are included. Notably, as the hydrogenation temperature increased, the position of the (101) peak shifted slightly toward higher 2θ values, from 25.30° for the Ru-TNT (H500) sample to 25.32° for the Ru-TNT (H600) sample, accompanied by a decrease in the FWHM value from 0.43° to 0.39°. Therefore, the crystallite size along the (101) plane increased from 20.2 to 22.2 nm. It is noteworthy that, for the Ru-TNT (H600) sample, the crystallite size along the (110) plane at a $2\theta = 27.47°$, associated with the rutile phase, was determined to be 24.8 nm, which is notably larger than the crystallite size along the (101) plane.

Table 1. The position of the main diffraction peaks, the full width at half maximum (FWHM), crystallite size, and d-spacing of Ru-TNT samples before and after thermal hydrogenation treatment at 500, 550, and 600 °C

Sample name	2θ (°)	A: Anatase R: Rutile	FWHM (°)	D (nm)	d-spacing (Å)
Ru-TNT (H500)	25.30	(101)/A	0.43	20.2	3.517
Ru-TNT (H550)	25.31	(101)/A	0.39	22.2	3.516
Ru-TNT (H600)	25.32	(101)/A	0.39	22.2	3.515
Ru-TNT (H600)	27.47	(110)/R	0.35	24.8	3.244

The full width at half maximum (FWHM) of Ru-TNT (H550) and Ru-TNT (H600) was observed to be smaller than that of the Ru-TNT (H500) sample, suggesting that higher hydrogenation temperatures induce internal stress.[28]

From Table 1, the thermal hydrogenation treatment of Ru-doped TiO_2 nanotubes reduced the d-spacing value as a result of oxygen vacancy defects introduced into the crystal structure of the samples.[29] It is worth mentioning that the incorporation of Ru ions into the TNTs lattice could increase d-spacing value, causing a shift in the XRD peaks toward lower angles. This occurs because of the slightly larger effective ionic radius of Ru^{4+} (0.62 Å) compared to Ti^{4+} (0.569 Å), while still maintaining the anatase framework.[30] A further novel finding of this study is that the hydrogenation process significantly influences the crystal structure and lattice parameters of titanium dioxide, surpassing the effects of ruthenium doping at lower doping concentrations.

As discussed, the XRD patterns of hydrogenated Ru-doped TiO_2 samples revealed a transition from the anatase phase to a mixed anatase-rutile phase as the hydrogenation temperature exceeded 600 °C. The transformation of anatase to rutile is a significant phase transition in TiO_2, which influences its photocatalytic properties and applications such as water splitting and solar cells.[31,32] The intensity ratio (I_A/I_R) of the most prominent anatase reflection (101) to that of the strongest rutile reflection (110) for TNT samples remains unaffected by variations in diffractometer characteristics.[33] Consequently, this ratio serves as a valuable indicator of the samples' composition and anatase-to-rutile transition. Bar diagrams presented in Figure 4 display the intensity of I_A and I_R for the hydrogenated samples. The results indicate that the Ru-TNT (H500) and Ru-TNT (H550) samples have a minimal presence of rutile, whereas the Ru-TNT (H600) sample exhibits a significant quantity of the rutile phase.

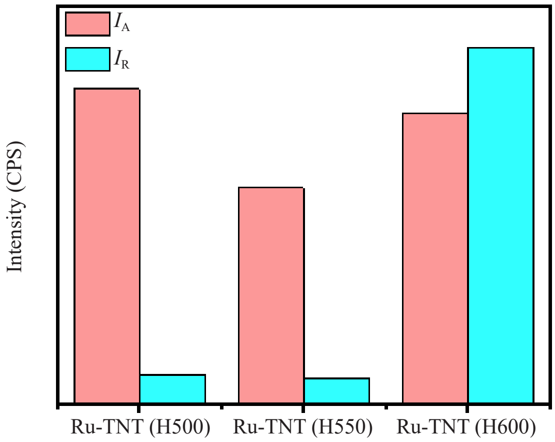

Figure 4. Bar diagrams depicting the intensity of the primary reflections for the anatase (I_A) and rutile (I_R) phases of hydrogenated Ru-TNTs

To assess the relative quantities of rutile and anatase phases in the samples, the weight fraction calculation can be utilized. The weight fraction of an anatase-rutile mixture can be determined by the method of Spurr and Myers as follows:[33]

$$W_A = \frac{1}{1 + 1.26\left(\frac{I_R}{I_A}\right)} \tag{3}$$

I_A and I_R represent the intensity of the (101) anatase peak and (110) rutile peak, respectively.

Table 2. The I_R/I_A intensity ratio, weight fraction of anatase (W_A), and W_A% derived from XRD data for hydrogenated samples at temperatures of 500, 550, and 600 °C

Sample name	I_R/I_A intensity ratio	Weight fraction of anatase (W_A)	W_A%
Ru-TNT (H500)	0.0963	0.8918	89.18
Ru-TNT (H550)	0.1245	0.8644	86.44
Ru-TNT (H600)	1.2217	0.3938	39.38

Table 2 summarizes the relationship between the I_R/I_A intensity ratio, the weight fraction of anatase (W_A) and the percentage weight fraction of anatase (W_A%) for three Ru-TNT samples treated at different hydrogenation temperatures (500 °C, 550 °C, and 600 °C). For the Ru-TNT (H500) sample, the I_R/I_A intensity ratio is 0.0963, indicating that the rutile phase is negligible compared to the anatase phase. In addition, the weight fraction of anatase is 0.8918, corresponding to 89.18% of the total sample weight. Therefore, the Ru-TNT (H500) sample consists predominantly of anatase, with minimal rutile content.

In the Ru-TNT (H550) sample, the I_R/I_A intensity ratio increased slightly to 0.1245, suggesting a gradual rise in the rutile phase. Consequently, W_A decreased to 0.8644, corresponding to 86.44% of the total weight. The increase in the rutile content at this temperature indicates the onset of the anatase to rutile phase transformation. Finally, the I_R/I_A intensity ratio rises significantly to 1.2217, indicating a major increase in rutile content in the Ru-TNT (H600) sample. Correspondingly, the weight fraction of anatase decreases sharply to 0.3938, confirming a substantial phase transition from anatase to rutile due to the higher hydrogenation temperature.

3.2 *Morphological alterations*

Field-emission scanning electron microscope (FE-SEM) was employed to examine the surface morphology of the fabricated thin films. As shown in Figure 5a, the Ru-TNT (H500) nanotubes exhibit a well-organized, densely packed structure with a uniform distribution. The clearly visible circular openings indicate that the anodization and thermal hydrogenation processes successfully preserved the structural integrity of the nanotubes.[34] The surface maintains a porous, tube-like structure, which is essential for applications such as photocatalysis and photoelectrochemical water splitting.[34,35]

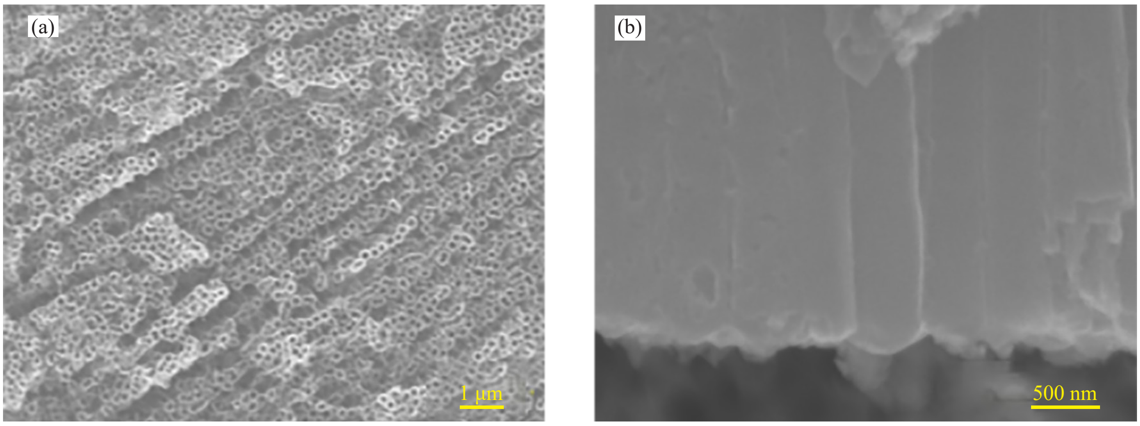

Figure 5. (a) Top-view and (b) cross-sectional view of FESEM images of Ru-TNT (H500) sample

The absence of significant deformation suggests that hydrogenation at 500 °C did not compromise the nanotube architecture. The cross-sectional view (Figure 5b) reveals vertically aligned nanotubes of uniform length, indicating an effective anodization process in which the tubes grow perpendicular to the substrate. The nanotube walls appear thin, consistent with anodized TiO_2 nanotubes.[36] The preservation of this feature during hydrogenation demonstrates the structural stability under thermal treatment at 500 °C. The nanotubes remain intact without signs of collapse or damage, highlighting their resilience under the applied hydrogenation conditions.

A comparative analysis of the cross-sectional FE-SEM images of Ru-doped TNTs subjected to thermal hydrogenation at 500, 550, and 600 °C is presented in Figure 6. The Ru-TNT (H500) nanotubes retain a well-ordered, vertically aligned structure. Their walls appear smooth and uniform, indicating minimal damage during hydrogenation. The overall structure remains intact, with distinct separation between individual nanotubes. This observation is consistent with previous research findings.[37,38]

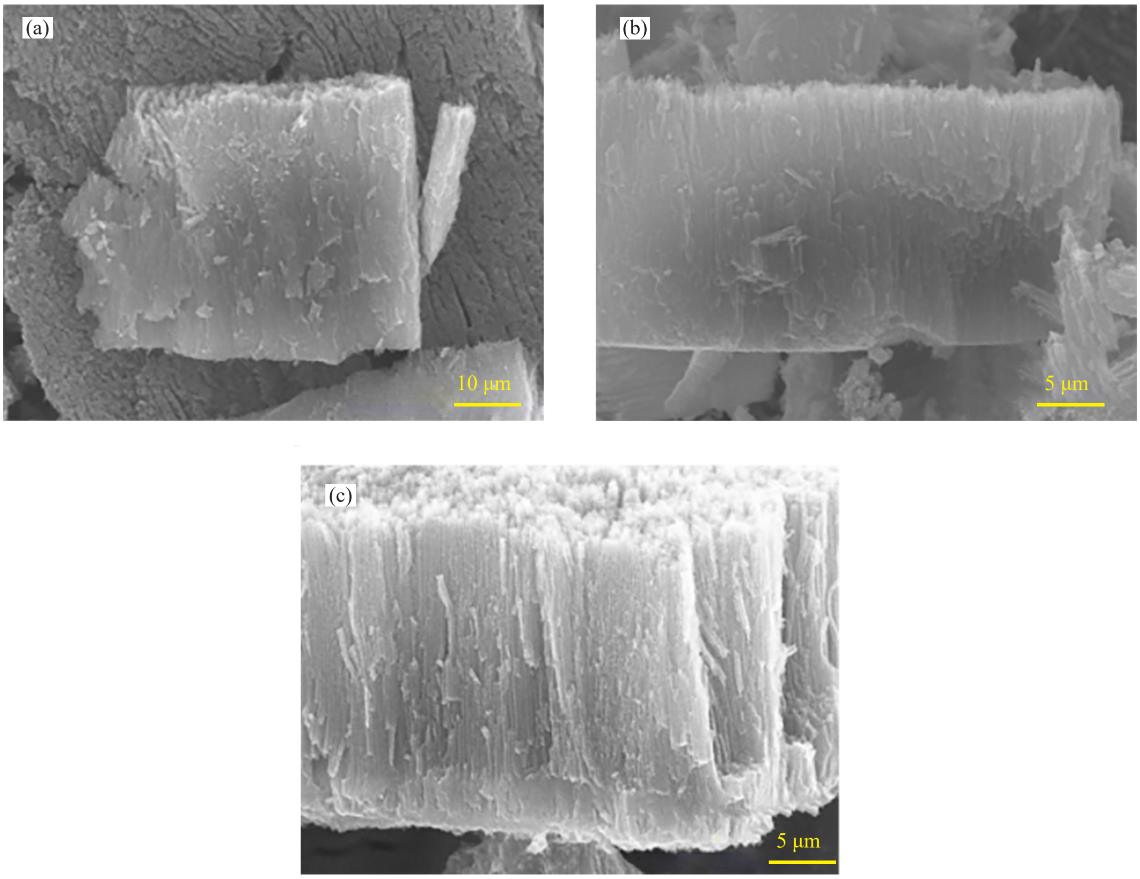

Figure 6. Cross-sectional FESEM images of (a) Ru-TNT (H500), (b) Ru-TNT (H550), and (c) Ru-TNT (H600), respectively

To the best of our knowledge, the anatase phase is expected to remain the dominant phase at this temperature, as temperatures up to 550 °C generally preserve anatase as the primary crystalline phase. This structural stability is highly beneficial for photocatalytic activity, as it maintains the integrity of the active sites, ensures efficient charge separation, and facilitates the transfer of photogenerated electrons and holes, ultimately enhancing the overall efficiency and durability of the photocatalytic process.[39,40] Compared to Ru-TNT (H500), the tube walls of Ru-TNT (H550) exhibit slight roughness, suggesting the initiation of phase transformation or structural modification. This roughening may be associated with the gradual emergence of the rutile phase. Additionally, partial deformation or irregularity at the tube ends could indicate localized stress induced by increasing temperature. At 550 °C, the anatase-to-rutile phase transition may initiate, leading to the observed morphological changes. This finding aligns with results from other studies, further validating the observed trends and reinforcing a shared understanding within the research community regarding this phenomenon.[41,42] However, the Ru-TNT (H600) nanotubes underwent significant structural changes. The tube walls became thicker and less defined, indicating a further phase transformation to rutile. Many tubes exhibited collapse or fusion, resulting in a loss of alignment. This deformation is likely attributed to the combined effects of thermal stress and hydrogenation at elevated temperatures. By 600 °C, the rutile phase is expected to dominate, as it is thermodynamically stable at high temperatures.[43,44]

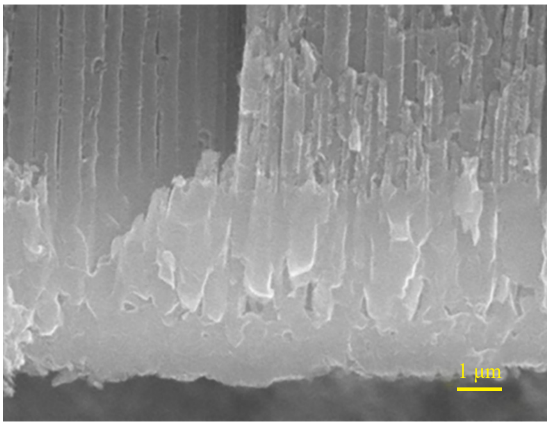

Figure 7. Cross-sectional FESEM image of Ru-TNT (H600) at higher magnification

As illustrated in Figure 7, this phase transition corresponds with the disappearance of distinct nanotube characteristics. The tubular architecture of Ru-TNT (H600) appears heavily deformed, with noticeable collapse and fusion of nanotube walls. This indicates a loss of the well-aligned nanotube structure typically observed at lower hydrogenation temperatures. The nanotubes' walls seem thickened, likely due to sintering effects induced by high thermal stress and phase transformation. These structural changes could reduce the material's surface area and porosity.[8,13] Furthermore, the bottom region of the nanotubes appears compacted, suggesting densification near the substrate due to prolonged exposure to elevated temperatures and hydrogenation.

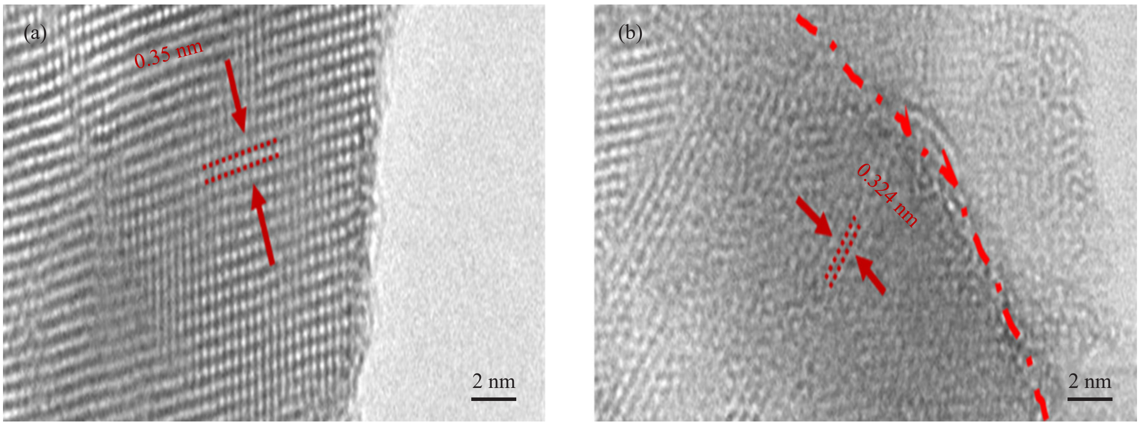

Figure 8. HRTEM images of (a) Ru-TNT (H500) and (b) Ru-TNT (H600), with the dotted line indicating the lattice distortion

Furthermore, the high-resolution transmission electron microscopy (HRTEM) images of Ru-TNT (H500) and Ru-TNT (H600) samples revealed significant morphological changes due to thermal hydrogenation treatment as detailed below:

- Ru-TNT (H500) Morphology: The Ru-TNT (H500) nanotubes exhibited a well-defined crystalline lattice characteristic of the anatase phase, with a lattice spacing of ~ 0.35 nm, as shown in Figure 8a.
- Ru-TNT (H600) Morphology: After hydrogenation at 600 °C, the morphology of the nanotubes underwent notable transformations. The HRTEM image in Figure 8b reveals a disordered outer layer (~ 4-5 nm thick), indicating structural changes by the hydrogenation post-treatment at 600 °C. This outer disordered layer exhibits increased defects and distortions, which are attributed to the high-temperature treatment, likely resulting in a decrease in structural stability and a phase transformation.
- Phase Transition and Lattice Distortions: In addition to the morphological changes, the hydrogenation process

induced lattice distortions in the material. The transition from the anatase to the rutile phase at 600 °C induced significant changes in the crystal structure, as observed in Figure 8b, where the lattice spacing corresponding to the rutile phase was measured at ~ 0.324 nm.

These findings, which are fully consistent with the results obtained from X-ray diffraction and field emission scanning electron microscopy, demonstrate that thermal hydrogenation not only alters the phase composition but also induces significant morphological deformations, such as lattice distortions. These modifications are critical for understanding the overall structural integrity and functionality of the TiO_2 nanotubes.

4. Conclusion

This study systematically explored the combined effects of ruthenium doping and thermal hydrogenation post-treatment on the structural and phase properties of TiO_2 nanotubes. The key findings are summarized as follows:

(1) Structural Stability & Phase Evolution: Ruthenium doping enhanced lattice stability and facilitated controlled phase transformation, particularly when combined with hydrogenation in an Ar/H_2 atmosphere at 500 °C, 550 °C, and 600 °C. Higher hydrogenation temperatures accelerated the anatase-to-rutile phase transition while inducing beneficial lattice distortions and defects.

(2) Morphological Transformations: At 500 °C, the nanotubes retained their well-organized architecture, crucial for functional applications. However, at elevated temperatures, significant morphological changes, such as wall thickening and partial fusion, were observed due to advanced phase transformation and thermal stress effects.

(3) Practical Implications: These findings provide valuable insights into engineering TiO_2 nanotubes with tailored properties for photocatalysis and energy conversion applications. The synergistic effects of Ru doping and thermal hydrogenation offer a promising strategy to enhance material performance, leading to more efficient and durable nanostructured systems.

Future research could explore different hydrogenation durations to study their effects on phase transitions and stability in Ru-doped TiO_2 nanotubes. Theoretical modeling, such as DFT calculations, may help understand phase transformations. Investigating long-term stability in real-world applications is essential, as well as exploring doping with other metals like platinum or palladium to expand potential applications. These directions could provide deeper insights and enhance material performance.

Acknowledgements

The authors thank Pasargad Institute for Advanced Innovative Solutions (PIAIS) for financial support of project number 10161.

Author’s contribution

Elham Khorashadizade: Conceptualization, methodology, validation, formal analysis, investigation, writing -original draft, review & editing, supervision. Fatemeh Nasiri: Investigation, schematic and graphical abstract preparation.

Conflict of interest

There are no potential competing interests.

References

[1] Lushaba, N. R.; Parani, S.; Maluleke, R.; Mbaz, G. I. M.; Oluwafemi, O. S. *Nano Futures* **2023,** *7*, 015003.

[2] Ruan, X.; Li, S.; Huang, C.; Zheng, W.; Cui, X.; Ravi, S. K. *Adv. Mater*. **2024,** *36*, 1-58.

[3] Lin, Z.; Pei, L.; Liu, S.; Jiang, X.; Xu, W.; Li, F.; Wu, X.; Wang, H.; Lu, X. J. *Water Process Eng*. **2025,** *70*, 106909.

[4] Balu, R.; Devendrapandi, G.; Gnanasekaran, L.; Karthika, P. C.; Abd-Elkader, O. H.; Kim, W. K.; Reddy, V. R. M.; Kapoor, M.; Singh, S.; Lavanya, M. *Sol. Energy Mater. Sol. Cells* **2025,** *279*, 113226.

[5] Jan, F. A.; Wajidullah; Ullah, R.; Salman; Ullah, N.; Salam, A. *Nano Futures* **2022,** *6*, 015003.

[6] Zhao, Y.; Shu, Y.; Linghu, X.; Liu, W.; Di, M.; Zhang, C.; Shan, D.; Yi, R.; Wang, B. *Chemosphere* **2024,** *346*, 140595.

[7] Zhang, Q.; Yao, C.; Zhang, F.; Chen, Y.; Li, Z.; Zhou, Y.; Qin, Y.; Xu, L.; Feng, F.; Zhao, J.; Lu, C.; Zhang, Q.; Wang, Q.; Li, X. *J. Mater. Chem. A*. **2025,** *13*, 5180-5190.

[8] Khorashadizade, E.; Mohajernia, S.; Hejazi, S.; Mehdipour, H.; Naseri, N.; Moradlou, O.; Moshfegh, A.; Schmuki, P. *J. Phys. Chem. C*. **2021,** *125*, 6116-6127.

[9] Ismael, M. *New J. Chem*. **2019,** *43*, 9596-9605.

[10] Xu, Z.; Yin, X.; Guo, Y.; Pu, Y.; He, M. *J. Mater. Chem. C*. **2018,** *6*, 4746-4752.

[11] Zheng, J.; Xia, R.; Yagoob, N.; Kaghazchi, P.; Elshof, J. E.; Huijben, M. *ACS Appl. Mater. Interfaces* **2024,** *16*, 8616-8626.

[12] Mohajernia, S.; Hejazi, S.; Andryskova, P.; Zoppellaro, G.; Tomanec, O.; Zboril, R.; Schmuki, P. *ChemElectroChem* **2019,** *6*, 1244-1249.

[13] Mohajernia, S.; Hejazi, S.; Mazare, A.; Nguyen, N. T.; Schmuki, P. *Chem.-Eur. J.* **2017,** *23*, 12406-12411.

[14] Talla, A.; Suliali, N. J.; Goosen, W. E.; Urgessa, Z. N.; Motloung, S. V.; Botha, J. R. *Phys. B Condens. Matter* **2022,** *640*, 411999.

[15] Pour-Ali, S.; Tavangar, R.; Namdar-Asl, H.; Esfandiari, N.; Khorashadizade, E. *J. Photochem. Photobiol., A* **2024,** *452*, 115586.

[16] Khorashadizade, E.; Arabi, H.; Yousefi, A. *Appl. Mech. Mater*. **2012,** *229-231*, 210-214.

[17] Patterson, A. L. *Phys. Rev*. **1939,** *56*, 978-982.

[18] Lim, D. J.; Marks, N. A.; Rowles, M. R. *Carbon* **2020,** *162*, 475-480.

[19] Ilyas, S.; Heryanto; Abdullah, B.; Tahir, D. *Nano-Struct. Nano-Objects* **2019,** *20*, 100396.

[20] Langford, J. I.; Wilson, A. J. C. *J. Appl. Cryst*. **1978,** *11*, 102-113.

[21] Wiranwetchayan, O.; Promnopas, S.; Thongtem, T.; Chaipanich, A.; Thongtem, S. *Surf. Coat. Technol*. **2017,** *326*, 310-315.

[22] Khorashadizade, E.; Mohajernia, S.; Hejazi, S.; Mehdipour, H.; Naseri, N.; Moradlou, O.; Liu, N.; Moshfegh, A.; Schmuki, P. *ChemElectroChem* **2020,** *7*, 1699-1706.

[23] Soundarrajan, P.; Sankarasubramanian, K.; Sethuraman, K.; Ramamurthi, K. *CrystEngComm* **2014,** *16*, 8756-8768.

[24] Khorashadizade, E.; Rahimi, K.; Mohajernia, S.; Hejazi, S.; Naseri, N.; Moradlou, O.; Moshfegh, A.; Schmuki, P. *Int. J. Hydrogen Energy* **2024,** *74*, 434-446.

[25] Allieta, M.; Coduri, M.; Naldoni, A. *Appl. Nano*. **2024,** *5*, 72-83.

[26] Samsudin, E. M.; Abd Hamid, S. B.; Juan, J. C.; Basirun, W. J.; Centi, G. *Appl. Surf. Sci*. **2016,** *370*, 380-393.

[27] Taneja, Y.; Dube, D.; Singh, R. *J. Mater. Chem. C* **2024,** *12*, 14774-147808.

[28] Harumoto, T.; Shi, J.; Nakamura, Y. *Int. J. Hydrogen Energy* **2020,** *45*, 11662-11674.

[29] Naldoni, A.; Altomare, M.; Zoppellaro, G.; Liu, N.; Kment, Š.; Zbořil, R.; Schmuki, P. *ACS Catal*. **2019,** *9*, 345-364.

[30] Ghosh, D. C.; Biswas, R. *Int. J. Mol. Sci*. **2003,** *4*, 379-407.

[31] Shymanovska, V. V.; Khalyavka, T. A.; Manuilov, E. V.; Gavrilko, T. A.; Aho, A.; Naumov, V. V.; Shcherban, N. D. *J. Phys. Chem. Solids* **2022,** *160*, 110308.

[32] Zhang, J.; Zhou, P.; Liu, J.; Yu, J. *Phys. Chem. Chem. Phys*. **2014,** *16*, 20382-20386.

[33] Spurr, R. A.; Myers, H. *Anal. Chem*. **1957,** *29*, 760-762.

[34] Hejazi, S.; Pour-Ali, S.; Killian, M. S.; Mohajernia, S. *Electrochem. Commun*. **2022,** *136*, 107246.

[35] Lee, K.; Mazare, A.; Schmuki, P. *Chem. Rev*. **2014,** *114*, 9385-9454.

[36] Roy, P.; Berger, S.; Schmuki, P. *Angew. Chem., Int. Ed*. **2011,** *50*, 2904-2939.

[37] Jo, S.; Im, S.; Weon, S.; Shin, H.; Lim, J. *Chem. Eng. J*. **2023,** *477*, 147031.

[38] Chen, J.; Xia, Z.; Li, H.; Li, Q.; Zhang, Y. *Electrochim. Acta*. **2015,** *166*, 174-182.

[39] Liu, N.; Chen, X.; Zhang, J.; Schwank, J. W. *Catal. Today* **2014,** *225*, 34-51.

[40] Camposeco, R.; Castillo, S.; Navarrete, J.; Gomez, R. *Catal. Today* **2016,** *266*, 90-101.

[41] Lu, R.; Wang, C.; Wang, X.; Wang, Y.; Wang, N.; Chou, J.; Li, T.; Zhang, Z.; Ling, Y.; Chen, S. *Int. J. Nanomed* **2018,** *13*, 2037-2049.

[42] Cheng, Q.; Wang, A.; Song, Z.; Bao, J.; Xue, J.; Wei, Y.; Li, S.; Lv, L.; Ding, J.; Cai, M.; Chen, J.; Wang, Q.; Gao, C.; Sun, S. *J. Environ. Chem. Eng*. **2021,** *9*, 105080.

[43] Hanaor, D. A. H.; Sorrell, C. C. *J. Mater. Sci*. **2011,** *46*, 855-874.

[44] Smith, S. J.; Stevens, R.; Liu, S.; Li, G.; Navrotsky, A.; Boerio-Goates, J.; Woodfield, B. F. *Am. Mineral*. **2009,** *94*, 236-243.